CrossMark
click for updates

Highly active MnOₓ–CeO₂ catalyst for diesel soot combustion†

Han Zhao,[ab] Xiaoxia Zhou,[a] Min Wang,[ab] Zhiguo Xie,[a] Hangrong Chen*[ac] and Jianlin Shi[ac]

A series of MnO_x–CeO_2 composites have been prepared *via* a facile coprecipitation method and used as catalysts for diesel soot combustion. It is found that the content of manganese oxide has a considerable influence on both the morphology and catalytic activity for diesel soot combustion in the copresence of NO_x and O_2. Superior catalytic activity ($T_f = 360\ °C$) was obtained over the optimized catalyst CM_{20} [Mn/(Mn + Ce) equals to 20 at%], which is believed to be attributable to the following two aspects: (1) the abundant pore structure, presenting between the loosely-packed homogeneous particles with similar sizes to that of the soot particles, which is beneficial for mass transfer and heat diffusion as well as the sufficient contact between catalyst and soot; (2) high concentration of Mn^{4+} and Ce^{3+} cations derived from the charge transfer between Mn and Ce species as active sites can adsorb and activate NO and O_2, and then greatly facilitate NO_2 production.

1. Introduction

Soot, as one of the main pollutants from diesel emission, has caused severe environmental problems like haze,[1] and several emission control strategies have been adopted to meet the demands of more and more stringent legislation, such as improvements in fuel oil,[2] modifications of the engine or process[3,4] and exhaust after-treatment systems.[5] For example, the diesel particulate filter (DPF) used in the after-treatment systems has so far been the most promising technological option. When the diesel exhaust flows through DPF, over 90% of the soot can be trapped and then be continuously or periodically combusted to CO_2.[6] However, the combustion temperature of soot (around 600 °C)[7] is far beyond the normal diesel exhaust temperature range (175–400 °C),[8] making the regeneration of DPF an intractable problem. Aimed at the passive regeneration of DPF, many kinds of catalysts, such as noble metals,[9] transition metal oxides,[10] perovskite and/or perovskite-like mixed oxides,[11] spinel mixed oxides,[12] alkaline metal/alkaline-earth metal oxides,[13] and the popular ceria-based oxides,[14–19] have

been developed to decrease the soot combustion temperature. Additionally, many researches demonstrate that the introduction of macropores or large voids into the catalysts can greatly facilitate the heat and mass transfer as well as improve the contact between soot and the catalysts, eventually to reach a high activity towards soot oxidation.[11,20–25] For example, Wei *et al.*[23] synthesized a three-dimensionally ordered macroporous (3DOM) $LaFeO_3$ catalyst loaded with tiny golden nanoparticles (∼2.9 nm), showing the temperature of maximum soot combustion rate (T_m) at 366 °C under loose contact mode between soot and catalyst. Recently, Nascimento *et al.*[25] synthesized $Ag/CeO_x/FeO_y$ catalysts supported on cordierite for the control of diesel soot emission, showing further decreased T_m (334 °C), and T_f (finishing soot combustion temperature, 400 °C), exhibiting great potential in application. However, the high-cost, the sensitivity to sulfur, and easily sintering characteristic of noble metal catalysts,[26,27] as well as the difficulty in the synthesis of 3DOM materials hinder the industrial application of this kind of catalysts.

MnO_x–CeO_2 composites have been widely used in many catalytic reaction processes, such as wet oxidation of toxic organic pollutants[28] and oxidation of gaseous[29] or even liquid pollutants,[30] and proved to be a promising substitute for noble metal catalysts. But for catalytic soot combustion, the previously reported approaches are still hard to achieve a satisfactory performance on MnO_x–CeO_2 composites, *i.e.*, $T_m = 393$–420 °C, $T_f > 400$ °C, maybe due to the unsufficient catalyst–soot contact that will restrict the full use of the active sites of the catalysts.[10,31–34]

Herein, a series of MnO_x–CeO_2 composites was synthesized through a facile modified coprecipitation method. Especially,

[a]*State Key Laboratory of High Performance Ceramics and Superfine Microstructure, Shanghai Institute of Ceramics Chinese Academy of Sciences, 1295 Ding-Xi Road, Shanghai 200050, P. R. China. E-mail: hrchen@mail.sic.ac.cn*

[b]*University of Chinese Academy of Sciences, Beijing, 100049, P. R. China*

[c]*Jiangsu National Synergetic Innovation Center for Advanced Materials (SICAM), Nanjing, P. R. China*

† Electronic supplementary information (ESI) available: Catalytic performance of samples reported in literatures together with CM_{20}, and NULL as reference; SEM images of MnO_x, CM_y ($y = 66$, 50 and 5), CeO_2 and soot; N_2 adsorption/desorption isotherms & pore size distributions of CM_{20} and CM_{33}; structural properties and H_2-TPR profiles of all the catalysts studied, SEM-EDS results of different areas in CM_{33}. See DOI: 10.1039/c6ra25738k

the optimized catalyst CM_{20} [Mn/(Mn + Ce) = 20 at%] shows uniform particle morphology with hierarchically porous structure which is much beneficial to the sufficient contact between catalyst and soot, as well as the high concentration of Mn^{4+}–Ce^{3+} cations on the surface that favors NO_2 production, thus exhibiting an excellent catalytic activity for the removal of soot in NO_x/O_2 atmosphere, i.e., ignition temperature $(T_i) = 280\,°C$, $T_m = 326\,°C$ and $T_f = 360\,°C$. The possible catalytic mechanism for the soot combustion is also proposed.

2. Experimental

2.1 Catalyst preparation

All the chemicals used in this study were of analytical grade, and were used without further purification. MnO_x–CeO_2 composites were prepared by the co-precipitation method reported before[35] with some modification. A typical preparation procedure is as follows: firstly, 7.5 mmol nitrate including $Ce(NO_3)_3 \cdot 3H_2O$ and $Mn(NO_3)_2$ (50 wt% in aqueous solution) was dissolved in 30 mL deionized water. Then, 30 mL water solution including 30 mmol $NaHCO_3$ was quickly poured into the nitrate solution and the mixture was stirred for 30 min at room temperature. Next, the precipitates were filtered and washed with deionized water and ethyl alcohol alternately for several times. After drying at 100 °C, the precursors were grinded and then calcined under static air at 500 °C for 2 h with a heating rate of 1 °C min^{-1}. The obtained catalysts were designated CM_y, where y (%) is the Mn/(Mn + Ce) atomic ratio in the recipe. In addition, we prepared two single oxides (CeO_2 and MnO_x) for reference with the same synthesis condition.

2.2 Catalyst characterization

The nitrogen adsorption and desorption curves were obtained using Micromeritics Tristar 3000 at 77 K, and the specific surface area and the pore size distribution were calculated using the Brunauer–Emmett–Teller (BET) and Barrett–Joyner–Halenda (BJH) methods, respectively. Powder X-ray diffraction (XRD) patterns of the prepared samples were got using a Rigaku D/Max 2200 PC diffractometer with Cu Kα radiation (40 kV and 40 mA). Field emission scanning electron microscopy (FE-SEM) imaging was performed using Hitachi S-4800. Transmission electron microscopic (TEM) images, selected area electron diffraction (SAED) patterns and element mapping images were obtained using a JEOL-2010F electron microscope operated at 200 kV. X-ray photoelectron spectroscopy (XPS) signals were recorded using an ESCAlab 250 instrument. The fitting of the Mn element was carried out using Gaussian fitting parameters. The temperature-programed reduction with hydrogen (H_2-TPR) experiments were performed using a Micromeritics Chemisorb 2750 instrument in a 5% H_2/N_2 flow (25 mL min^{-1}) using 50 mg catalyst with a heating rate of 10 °C min^{-1}. The uptake amount of H_2 was measured using a thermal conductivity detector (TCD).

2.3 Activity testing

Carbon black from Degussa (diameters: 10–50 nm) was used as the model soot particles. Following a well-accepted procedure,

soot (10 mg) and catalyst (100 mg) were carefully mixed for 20 min with a spatula to simulate the loose contact mode, then silica pellets (1 g) were added and mixed by the spatula for another 10 min. It is worth noting that silica pellets were added to avoid pressure drop and favor heat transfer.[36] A gas mixture of 500 ppm NO, 10% O_2 and balance N_2 was feed with a flow rate of 200 mL min^{-1}. The space velocity was thus calculated to be 120 000 mL (g h)$^{-1}$. Afterwards, the mixture was heated to 650 °C at a heating rate of 5 °C min^{-1} in a tube furnace equipped with a thermal couple. To minish the error of the measurement to a least extent, the temperature of the tube furnace was monitored with a standard thermal couple, every gas flow was verified with a mechanical flow meter and the concentration of NO_x was measured by a NO_x analyzer (Thermo Fisher 42i-LS). The analysis of the emissions from the reactor was performed using an online GC-FID analyzer (GC2060 from Shanghai Ruimin Instrument Corp. Ltd.) equipped with a methane converter. The catalytic activities (conversion and selectivity) were calculated as indicated in previous reports in the literature, in terms of T_i, T_m and T_f values, which were respectively defined as the temperatures at 10%, 50% and 90% of soot conversion, and selectivity to CO_2 as well, which was quantified: selectivity (%) = S_{CO_2}(total)/$[S_{CO}$(total) + S_{CO_2}(total)], where S_{CO_x}(total) represents the area under the CO_x–temperature curve in the range of RT – 650 °C (x = 1 or 2).[37,38]

3. Results and discussion

3.1 Catalytic activity measurements

Fig. 1 shows the catalytic activity of the CM_y composites, references MnO_x and CeO_2, and NULL (without catalyst) towards soot oxidation under loose contact mode. It is obvious that compared with NULL, all the CM_y composites and the references MnO_x, CeO_2 show much lower characteristic temperatures and higher selectivity to CO_2 in the soot oxidation. Thereinto, CM_{20} shows the lowest characteristic temperatures ($T_i = 280\,°C$, $T_m = 326\,°C$, and $T_f = 360\,°C$) as well as the highest selectivity to CO_2 (95.6%), indicating that the interaction between Mn and Ce species can greatly improve the catalytic activity toward the soot oxidation. Even compared with the noble-metal based catalysts supported on 3DOM oxides or
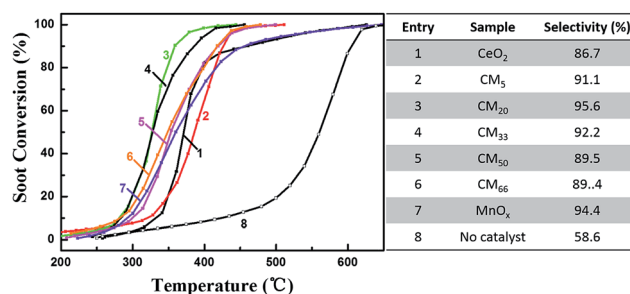

Entry	Sample	Selectivity (%)
1	CeO_2	86.7
2	CM_5	91.1
3	CM_{20}	95.6
4	CM_{33}	92.2
5	CM_{50}	89.5
6	CM_{66}	89..4
7	MnO_x	94.4
8	No catalyst	58.6

Fig. 1 Catalytic activity (left) and selectivity to CO_2 (right) for soot combustion over different catalysts or NULL (without catalyst) under loose contact mode. Reaction conditions: 500 ppm NO and 10% O_2 in N_2 with a total flow of 200 mL min^{-1}, mass of soot–catalyst–silica is 10–100–1000 mg.

cordierite, as well as the MnO_x–CeO_2 catalysts prepared by other methods, CM_{20} still shows much lower characteristic temperatures (especially T_f) for soot combustion under similar reaction conditions (loose contact mode, shown in Table S1†). It should be noted that even at a higher space velocity [330 000 mL (g_{catal} h)$^{-1}$, the highest one among those shown in Table S1†], CM_{20} still shows a much lower T_m value (350 °C) than that of other reported MnO_x–CeO_2 catalysts (393–420 °C) shown in Table S1.† Fig. S1 and S2† indicates good stability in both catalytic activity and structure for these CM_y composite catalysts (herein, CM_{33} was chosen as an example). In order to understand the different catalytic performances on these prepared catalysts, XRD analysis, N_2 adsorption/desorption analysis and SEM/TEM observations were conducted to reveal both the phase composition and the morphology/pore structure of different catalysts.

3.2 XRD analyses

Fig. 2 shows the XRD patterns of different CM_y composites and the references MnO_x and CeO_2. It is found that the reference CeO_2 exhibits a single phase of cubic CeO_2 (JCPDS 43-1002), while MnO_x shows three distinguishable manganese oxides of Mn_2O_3 (JCPDS 73-1826), MnO_2 (JCPDS 72-1982) and Mn_5O_8 (JCPDS 39-1218). In addition, compared with reference CeO_2, all the CM_y composites show relatively wide diffraction peaks corresponding to cubic CeO_2 phase, without detectable Mn-containing phases or obvious peak shift, indicating that manganese oxides may exist in the form of highly dispersive and/or amorphous species, thus decreasing the crystallinity of CeO_2. More interestingly, CM_{20} shows the biggest FWHM (the full width at half maximum) values of the main XRD peaks among all the CM_y composites, suggestive of the smallest crystalline grain according to the Scherrer equation, and the corresponding most abundant surface defect sites, which are beneficial for the improvement of catalytic activity.

3.3 SEM & TEM measurements for CM_{20}

The typical SEM images and the corresponding EDS spectrum, as well as TEM image and the corresponding element mapping
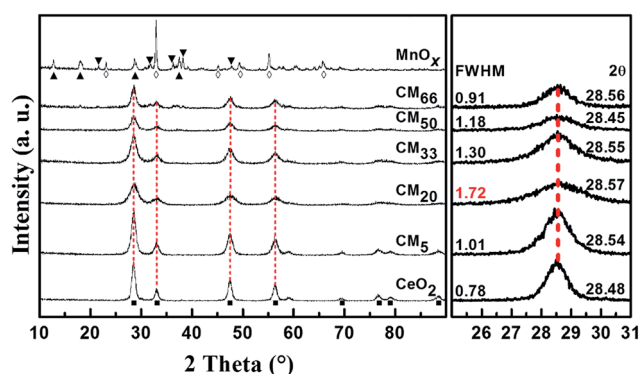
of CM_{20} shown in Fig. 3 indicate that CM_{20} is solely composed of uniform particles with loose packing, leaving abundant large pores, as indicated by the arrows in Fig. 3b, which is very different from the morphologies of all the other studied catalysts in Fig. S3† (CeO_2, CM_5, CM_{50}, CM_{66} and MnO_x). The pore sizes in CM_{20} are measured to be within 16–103 nm (Fig. 3b), which are consistent with its pore size distribution (10–159 nm) by N_2 adsorption/desorption analysis shown in Fig. S4† and summarized in Table S2.† As can be seen in Table S2,† the specific surface areas of CM_y composites are all larger than that of reference MnO_x and CeO_2. Especially, CM_{20} shows much enlarged specific surface area and pore volume as well. Besides, its pore size is also broadened. It is believed that the similar particle size of the sample CM_{20} to that of soot particles (Fig. S3-f†), and the abundant large pores in CM_{20} are both helpful to its sufficient contact with soot. Also, its high specific surface area and pore volume both favor the dispersion of active sites, thus making a great contribution to catalytic oxidation of soot. The atomic ratio of Mn/(Mn + Ce) is calculated to be 21.9%, according to EDS spectrum in Fig. 3c, similar to that of the starting solution. As can be found in Fig. 3d–f, both the Ce species and Mn species are homogeneously distributed in the prepared composite, indicating that manganese species shows highly dispersive with ceria species. The H_2-TPR results (Fig. S5†) confirm the interaction between Mn and Ce species in CM_y composites. Especially, CM_{20} shows excellent redox activity, which can be mainly attributed to the interaction between Ce and Mn species, inducing the changes of the local atomic environment for each element, as detected by the following XPS measurements.

3.4 XPS measurements

Fig. 4 shows the Mn 2p, Ce 3d and O 1s XPS spectra of the series of CM_y composites, as well as the references MnO_x and CeO_2. The analysis results of different samples are summarized in Table 1, based on the careful peak fitting procedure. The O 1s XPS spectra of the sample CM_y and the references MnO_x and CeO_2 can be deconvoluted into two components after Gaussian fitting, as shown in Fig. 4c, which can be ascribed to lattice oxygen O_{latt} (529.6 eV) and adsorbed oxygen O_{ads} (532.4 eV), respectively. Generally, adsorbed oxygen species always correspond to the numbers of oxygen vacancies,[39] which are beneficial for the activation of gaseous oxygen molecules in the feed gas. The existence of oxygen vacancies in CM_y can also be evidently confirmed by the results of Raman spectroscopy analysis (Fig. S6†). Compared with reference CeO_2, the main peak in the Raman spectra of CM_y, the F_{2g} mode of CeO_2 shows a distinct red-shift from 464 to (433–452) cm^{-1}, indicating that the interaction between Mn and Ce disturbed the fluorite-like structure to some extent and resulted in the formation of the oxygen vacancies in the CeO_2 lattice.[40] It is noting that the peak at 652 cm^{-1} for MnO_x also shifts down to (605–637) cm^{-1} for CM_y composites, which could also be related to the formation of oxygen vacancies in CM_y.[40] Usually, the high ratio of O_{ads}/O_{latt} indicates a high activity toward oxidation reaction. But in the present work, CM_{20}, though with the lowest O_{ads}/O_{latt} ratio

Fig. 2 XRD patterns of different CM_y composites and the references MnO_x and CeO_2 (left), (■-CeO_2; ◇-Mn_2O_3; ▲-MnO_2; ▼-Mn_5O_8), and the enlarged region between 25° and 31° of the patterns showing the corresponding FWHM values and peak positions of 2θ (right).
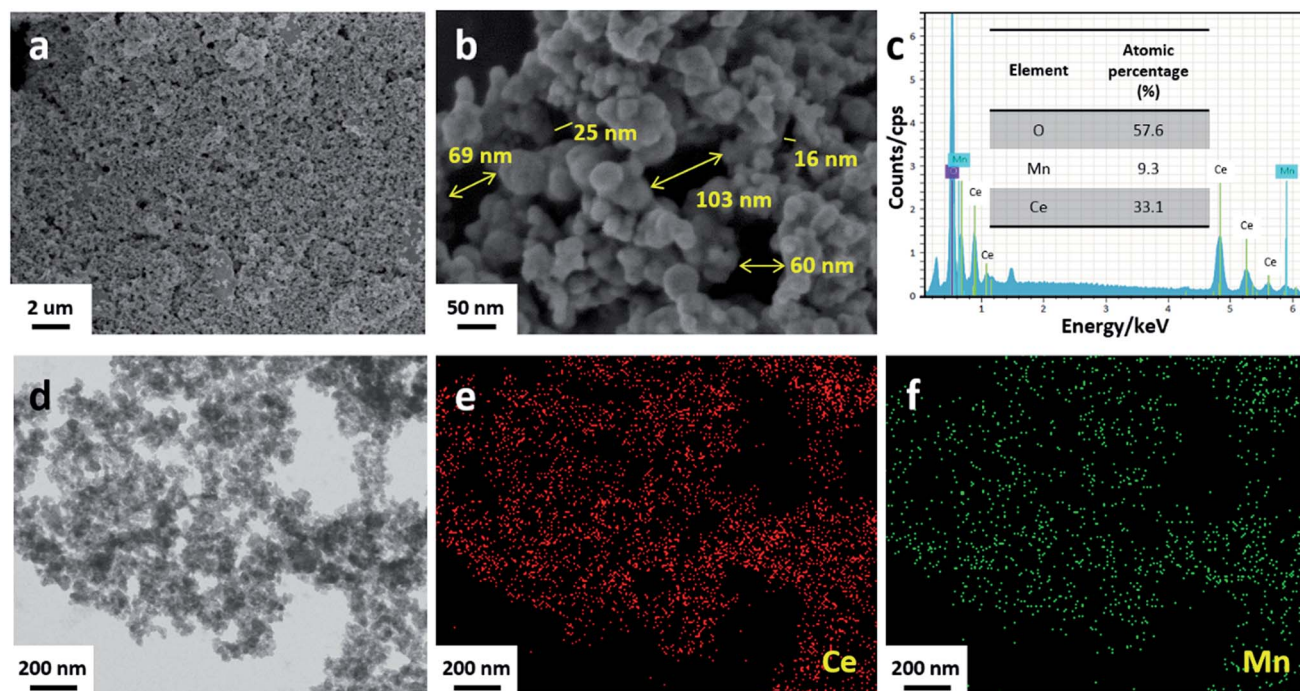
Fig. 3 Low-magnification SEM image (a), high-magnification SEM image (b), EDS spectrum (c), typical TEM image (d) and the element mapping (e and f) of CM_{20}.
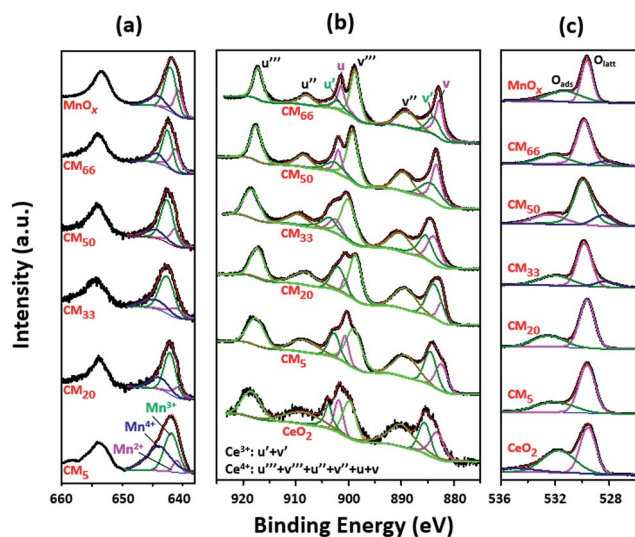

Fig. 4 XPS spectra of (a) Mn 2p, (b) Ce 3d and (c) O 1s for all CM_y composites and the reference MnO_x and/or CeO_2.

Table 1 XPS surface composition analysis of CM_y composites and the references MnO_x and/or CeO_2

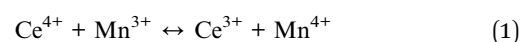| Sample	$O_{ads}/(O_{ads} + O_{latt})$ (%)	$Mn^{2+}/Mn^{3+}/Mn^{4+}$ (%)	$Ce^{3+}/(Ce^{3+} + Ce^{4+})$ (%)
MnO_x	54.9	27.5/52.1/20.3	
CM_{66}	33.3	35.2/48.7/16.1	17.3
CM_{50}	31.1	22.1/56.9/21.1	19.2
CM_{33}	30.5	20.1/58.5/21.3	24.9
CM_{20}	21.2	16.0/54.9/29.0	27.6
CM_5	27.7	8.0/56.8/35.1	22.0
CeO_2	46.6		18.2

among all the studied catalysts, still shows the highest catalytic activity for soot combustion in NO_x/O_2, which suggests that there exists another key factor besides adsorbed oxygen species determining the catalytic activity.

As shown in the Fig. 4 and Table 1, both Mn and Ce species present various valence states. Thereinto, it is found that the ratio of $Ce^{3+}/(Ce^{3+} + Ce^{4+})$ firstly increases and then decreases with the increase of y in CM_y, and the value reaches to a maximum value of 27.6% in CM_{20}, which indicates the charge

transfer between Mn and Ce within the interface (eqn (1)), as supported by the previous reports demonstrating negative charge transfer either from Mn to Ce or from Ce to Mn.[41–45] Such a charge transfer will lead to the strong interaction between Ce and Mn species and thus the formation of uniform nanoparticles.[46] This strong interaction between Mn and Ce can also be reflected in the results of H_2-TPR profiles shown in Fig. S5,† in which, all of the CM_y composites especially CM_{20} and CM_{33} show much lower reduction peak temperature than that for either MnO_x or CeO_2. Additionally, it is reported that the Mn^{4+} and Ce^{3+} can absorb and activate NO and O_2,[47,48] thus the Mn^{4+} and Ce^{3+} cations could serve as active sites for the catalytic soot combustion in NO_x/O_2 atmosphere, by promoting the formation of NO_2.

$$Ce^{4+} + Mn^{3+} \leftrightarrow Ce^{3+} + Mn^{4+} \qquad (1)$$

To further verify the role of Mn^{4+} and Ce^{3+} cations in the catalytic soot oxidation, a parameter "Ω" (defined in eqn (2)) was introduced to quantify the concentration of Mn^{4+} and Ce^{3+} cations in the CM_y composites.

$$\Omega = a \times b \qquad (2)$$

Where $a = (1 - y)[Ce^{3+}/(Ce^{3+} + Ce^{4+})]$, $b = y[Mn^{4+}/(Mn^{2+} + Mn^{3+} + Mn^{4+})]$, and y is that in CM_y. Moreover, the relationship between "Ω" value and the catalytic activity over the different catalysts CM_y are shown in Fig. 5. It is found that for the CM_y composites, the larger Ω value is, the higher catalytic activity is, which confirms the role of Mn^{4+} and Ce^{3+} cations as active sites for catalytic soot combustion in NO_x/O_2 over CM_y composites. Nevertheless, the sample CM_{66} seems an exception with a lower Ω value, showing higher catalytic activity than CM_{50}, which can be ascribed to the higher specific surface area and pore volume of CM_{66} (72 $m^2\ g^{-1}$ and 0.22 $cm^3\ g^{-1}$, Table S2†) than those of CM_{50} (53 $m^2\ g^{-1}$ and 0.11 $cm^3\ g^{-1}$, Table S2†).

3.5 SEM and TEM measurements for CM_{33}

It is worth noting that, compared with CM_{20}, CM_{33} shows a little lower catalytic activity and Ω value, and similar specific surface area but significantly lower pore volume. Therefore, the TEM and SEM analyses for CM_{33} were further performed, as shown in Fig. 6. It can be found that very different from the homogeneous morphology of CM_{20} particles shown in Fig. 3, CM_{33} shows some complex morphology in addition to the highly dispersive particles, such as micro-flakes (1 in Fig. 6c) and microspheres (3 in Fig. 6c). These two kinds of morphologies can also be found in the Ce-rich samples (CeO_2 and CM_5 in Fig. S3†), and the Mn-rich samples (CM_{50}, CM_{66} and MnO_x in Fig. S3†), respectively. Apparently, either the micro-flakes or the microsphere morphology in CM_{33} lacks the porous structure, thus leading to the lower pore volume than CM_{20} (Table S2†), which can strongly affect the efficient contact between catalyst and soot
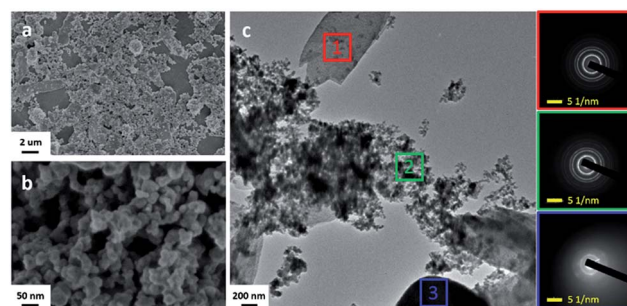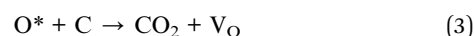

Fig. 6 Low-magnification SEM image (a), high-magnification SEM image (b), TEM image (c) of CM_{33}, and the corresponding SAED patterns to the different areas in (c).

particles and decrease the activity for soot oxidation. Nevertheless, the main component in CM_{33} still presents similar size and chemical composition (Fig. 6b, 2 in Fig. 6c and S7†) to CM_{20} particles (Fig. 3), thus it remains higher catalytic activity than other reference samples. Therefore, it is reconfirmed that the homogeneous particles morphology with hierarchically porous structure is one of the key factors in the catalytic process of soot oxidation.

Overall, the catalytic activity for soot oxidation in NO_x/O_2 atmosphere can be ascribed to the following two aspects: (1) abundant Mn^{4+} and Ce^{3+} cations (large Ω value) serve as active sites by promoting NO_2 production, e.g., CM_{20} with the largest Ω value ($\Omega = 128$) shows the best activity toward the soot oxidation. (2) The high surface area and pore volume as well as the typical morphology of the particles with hierarchically porous structure could improve the dispersion of active species and soot diffusion, e.g., CM_{66} with a lower Ω value ($\Omega = 62$) exhibits a relatively high activity for soot oxidation due to its high specific surface area and pore volume.

3.6 A possible catalytic mechanism for soot oxidation

Based on the above results and analyses, a possible mechanism for the catalytic soot combustion in NO_x/O_2 over the sample CM_{20} was proposed, as shown in Scheme 1. In this catalytic reaction, the efficient contact between the catalyst and soot, and the abundant active Mn^{4+}–Ce^{3+} species are two crucial issues determining the excellent catalytic performance. Generally, soot combustion over catalyst in NO_x/O_2 atmospheres is believed to follow two different pathways:[49] (i) direct soot combustion by surface active oxygen species, (ii) NO-aided soot combustion. In Route (i), oxygen species absorbed and activated by oxygen vacancies (V_O) on the catalyst surface can directly oxidize soot into CO_2 (reaction (3), where O* is the active oxygen species).[50]

$$O^* + C \rightarrow CO_2 + V_O \qquad (3)$$

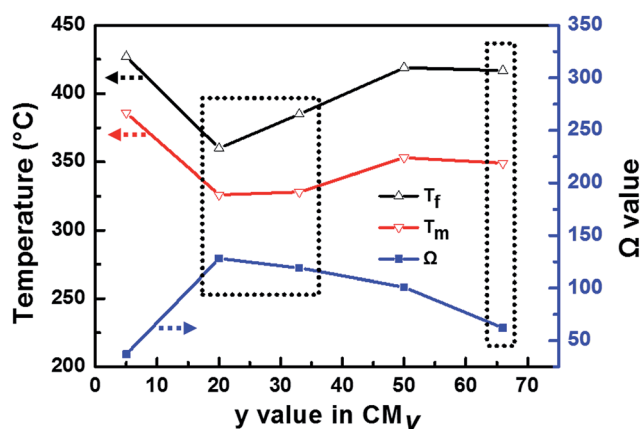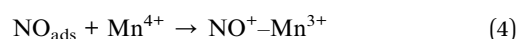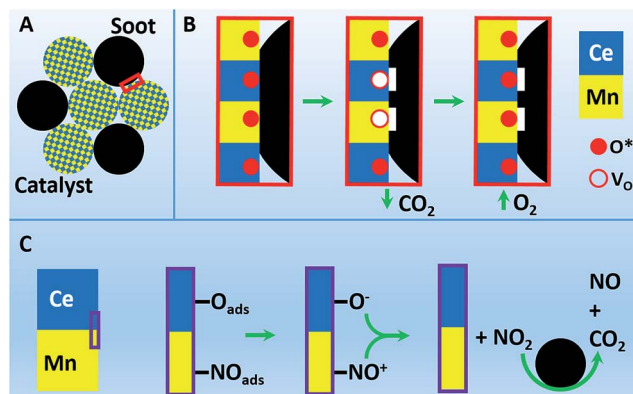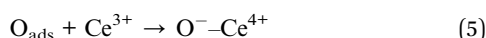While in Route (ii), the NO-aided soot combustion can be expressed as the following reactions:

Fig. 5 The different characteristic temperatures (T_m and T_f) and values of "Ω" as a function of y in CM_y. Reaction conditions for catalytic soot combustion: 500 ppm NO and 10% O_2 in N_2 with a total flow of 200 mL min^{-1}, mass of soot–catalyst–silica is 10–100–1000 mg, under loose contact mode.

$$NO_{ads} + Mn^{4+} \rightarrow NO^+ - Mn^{3+} \qquad (4)$$

Scheme 1 Schematic illustration of (A) the sufficient mixing of CM_{20} and soot particles, and the possible pathways of soot combustion on CM_{20} in NO_x/O_2: (B) Route (i): direct soot combustion by surface active oxygen species; (C) Route (ii): NO-aided soot combustion.

$$O_{ads} + Ce^{3+} \rightarrow O^- - Ce^{4+} \quad (5)$$

$$NO^+ - Mn^{3+} + O^- - Ce^{4+} \rightarrow NO_2 + Mn^{3+} + Ce^{4+} \quad (6)$$

$$NO_2 + C \rightarrow CO_2 + NO \quad (7)$$

As supported by previous reports, it can be rationally deduced that the abundant Mn^{4+} and Ce^{3+} cations in CM_{20} play different roles in the catalytic process. Therein, Mn^{4+} could adsorb and activate NO into active species NO^+, as shown in reaction (4);[47] while Ce^{3+} could activate the absorbed oxygen O_{ads} into O^- (reaction (5)).[48] Such resultant NO^+ and O^- species will react with each other to form NO_2 at the interface between Ce and Mn oxides (reaction (6)),[51] meanwhile, the produced $Ce^{4+} - Mn^{3+}$ will react through reaction (1) to recover the active site $Ce^{3+} - Mn^{4+}$, thus completing the catalysis cycle. Then in

reaction (7),[52] the produced NO_2, as a stronger oxidant than O_2, can be reduced back to NO by soot, which meanwhile can be oxidized to CO_2 at low temperatures. In order to further confirm the role of NO_x in the catalytic soot oxidation process, the temperature-programed oxidation of NO over CM_{33} with or without soot was further investigated, as shown in Fig. 7. It was found that with the addition of soot into the catalytic NO oxidation system, the NO_2 proportion in NO_x ($= NO + NO_2$) decreases in temperature range 200–400 °C, especially in the range of 300–375 °C, where the CO_2 concentration reaches its peak values. This coincidence confirms the reaction between NO_2 and C, which facilitates CO_2 production at the expense of NO_2 (reaction (7)). Moreover, catalysis activity measurement over CM_{20} without the presence of NO was also conducted for comparison to the case with NO existing in the feed gas, as shown in Fig. S8,† clearly demonstrating the positive effect of NO on the catalytic activity towards soot oxidation.

4.   Conclusions

In summary, a facile co-precipitation method has been adopted to prepare a series of MnO_x–CeO_2 composites for the catalytic oxidation of soot in the simulated diesel emission. Thereinto, the optimized CM_{20} shows the highest catalytic activity ($T_f = 360$ °C), under loose contact mode. The excellent catalytic activity can be attributed to its uniform particle morphology with hierarchically porous structure and the rich active Mn^{4+} and Ce^{3+} cations resulting from the suitable doping amount of Mn, which greatly accelerate soot oxidation in NO_x/O_2. A possible mechanism was proposed to interpret the role of Mn^{4+}–Ce^{3+} species as well as the active oxygen species in the catalytic process of soot combustion in NO_x/O_2. The MnO_x–CeO_2 composites prepared by this low-cost and easily-scalable method could find the promising practical application in the catalytic removal of soot in the diesel exhaust.

Acknowledgements

Notes and references

1 H. Horvath, *Atmos. Environ.*, 1993, **27**, 293–317.
2 L. L. N. Guarieiro, A. F. de Souza, E. A. Torres and J. B. de Andrade, *Atmos. Environ.*, 2009, **43**, 2754–2761.
3 Z. Gao and W. Schreiber, *Proc. Inst. Mech. Eng., Part D*, 2002, **216**, 619–628.
4 D. B. Kittelson, *J. Aerosol Sci.*, 1998, **29**, 575–588.
5 D. Fino, *Sci. Technol. Adv. Mater.*, 2007, **8**, 93–100.
6 B. A. A. L. van Setten, M. Makkee and J. A. Moulijn, *Catal. Rev.: Sci. Eng.*, 2001, **43**, 489–564.
7 E. Obeid, L. Lizarraga, M. N. Tsampas, A. Cordier, A. Boréave, M. C. Steil, G. Blanchard, K. Pajot and P. Vernoux, *J. Catal.*, 2014, **309**, 87–96.
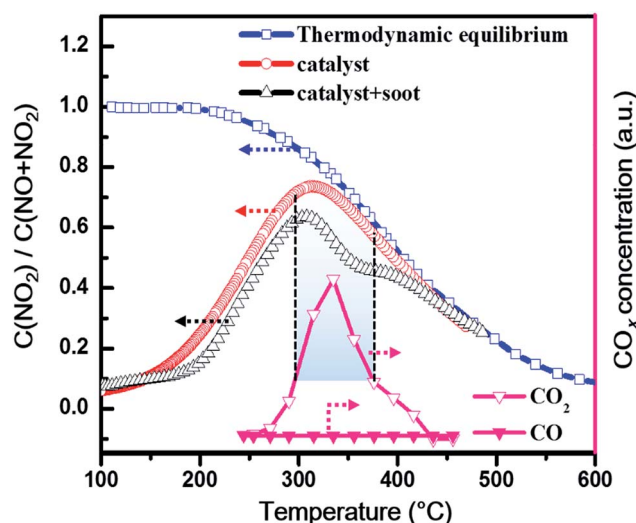
Fig. 7   The temperature-programed oxidation of NO over CM_{33} with or without soot under loose contact mode. Reaction conditions: 500 ppm NO and 10% O_2 in N_2 with a total flow of 200 mL min^{-1}, the mass of (soot−)catalyst−silica is (10−)100−1000 mg.

8 X. H. Yu, Z. Zhao, Y. C. Wei, J. Liu, J. M. Li, A. J. Duan and G. Y. Jiang, *Chin. J. Catal.*, 2015, **36**, 1957–1967.

9 J. O. Uchisawa, A. Obuchi, Z. Zhao and S. Kushiyama, *Appl. Catal., B*, 1998, **18**, L183–L187.

10 X. D. Wu, S. Liu, F. Lin and D. Weng, *J. Hazard. Mater.*, 2010, **181**, 722–728.

11 J. F. Xu, J. Liu, Z. Zhao, C. M. Xu, J. X. Zheng, A. J. Duan and G. Y. Jiang, *J. Catal.*, 2011, **282**, 1–12.

12 D. Fino, N. Russo, G. Saracco and V. Specchia, *J. Catal.*, 2006, **242**, 38–47.

13 L. Castoldi, R. Matarrese, L. Lietti and P. Forzatti, *Appl. Catal., B*, 2009, **90**, 278–285.

14 J. Liu, Z. Zhao, J. Q. Wang, C. M. Xu, A. J. Duan, G. Y. Jiang and Q. Yang, *Appl. Catal., B*, 2008, **84**, 185–195.

15 P. Sudarsanam, B. Hillary, B. Mallesham, B. G. Rao, M. H. Amin, A. Nafady, A. M. Alsalme, B. M. Reddy and S. K. Bhargava, *Langmuir*, 2016, **32**, 2208–2215.

16 S. Putla, M. H. Amin, B. M. Reddy, A. Nafady, K. A. Al Farhan and S. K. Bhargava, *ACS Appl. Mater. Interfaces*, 2015, **7**, 16525–16535.

17 P. Sudarsanam, K. Kuntaiaha and B. M. Reddy, *New J. Chem.*, 2014, **38**, 5991–6001.

18 P. Sudarsanam, B. Hillary, D. K. Deepa, M. H. Amin, B. Mallesham, B. M. Reddy and S. K. Bhargava, *Catal. Sci. Technol.*, 2015, **5**, 3496–3500.

19 P. Sudarsanam, A. Rangaswamy and B. M. Reddy, *RSC Adv.*, 2014, **4**, 46378–46382.

20 G. B. Zhang, H. R. Chen, Y. Gong, Z. Shu, D. N. He, Y. Zhu, X. X. Zhou, X. Q. Fan, H. J. Zhang and J. L. Shi, *Catal. Commun.*, 2013, **35**, 105–109.

21 E. D. Banus, V. G. Milt, E. E. Miro and M. A. Ulla, *Appl. Catal., B*, 2013, **132**, 479–486.

22 K. Krishna, A. Bueno-Lopez, M. Makkee and J. A. Moulijn, *Appl. Catal., B*, 2007, **75**, 189–200.

23 Y. C. Wei, J. Liu, Z. Zhao, Y. Chen, C. Xu, A. Duan, G. Jiang and H. He, *Angew. Chem., Int. Ed.*, 2011, **50**, 2326–2329.

24 C. M. Cao, Y. X. Zhang, D. S. Liu and M. Meng, *Small*, 2015, **11**, 3659–3664.

25 L. F. Nascimento, J. F. Lima, P. C. de Sousa Filho and O. A. Serra, *Chem. Eng. J.*, 2016, **290**, 454–464.

26 Y. Nagahara, S. Sugawara and K. Shinohara, *J. Power Sources*, 2008, **182**, 422–428.

27 I. Heo, J. W. Choung, P. S. Kim, I. S. Nam, Y. I. Song, C. B. In and G. K. Yeo, *Appl. Catal., B*, 2009, **92**, 114–125.

28 S. T. Hussain, A. Sayari and F. C. Larachi, *Appl. Catal., B*, 2001, **34**, 1–9.

29 D. Delimaris and T. Ioannides, *Appl. Catal., B*, 2008, **84**, 303–312.

30 X. Y. Wang, Q. Kang and D. Li, *Appl. Catal., B*, 2009, **86**, 166–175.

31 X. D. Wu, F. Lin, L. Wang, D. Weng and Z. Zhou, *J. Environ. Sci.*, 2011, **23**, 1205–1210.

32 M. L. Fu, K. L. Wang, R. P. Yu, X. E. Wen, M. Zhang, B. C. Huang, J. L. Wu, D. Q. Ye and H. Liang, *Chin. J. Inorg. Chem.*, 2012, **28**, 1593–1600.

33 H. L. Zhang, Y. Zhu, S. D. Wang, M. Zhao, M. C. Gong and Y. Q. Chen, *Fuel Process. Technol.*, 2015, **137**, 38–47.

34 F. Lin, X. D. Wu, S. Liu, D. Weng and Y. Y. Huang, *Chem. Eng. J.*, 2013, **226**, 105–112.

35 L. N. Cai, Z. H. Hu, P. Branton and W. C. Li, *Chin. J. Catal.*, 2014, **35**, 159–167.

36 X. D. Wu, F. Lin, H. B. Xu and D. Weng, *Appl. Catal., B*, 2010, **96**, 101–109.

37 J. Liu, Z. Zhao, J. Q. Wang, C. M. Xu, A. J. Duan, G. Y. Jiang and Q. Yang, *Appl. Catal., B*, 2008, **84**, 185–195.

38 A. L. Kustov and M. Makkee, *Appl. Catal., B*, 2009, **88**, 263–271.

39 S. H. Xie, Y. X. Liu, J. G. Deng, X. T. Zhao, J. Yang, K. F. Zhang, Z. Han and H. X. Dai, *J. Catal.*, 2016, **342**, 17–26.

40 X. M. Zhang, Y. Q. Deng, P. F. Tian, H. H. Shang, J. Xu and Y. F. Han, *Appl. Catal., B*, 2016, **191**, 179–191.

41 Z. Zeng and M. Greenblatt, *Phys. Rev. B: Condens. Matter Mater. Phys.*, 2001, **63**, 224410.

42 S. Imamura, *Ind. Eng. Chem. Res.*, 1999, **38**, 1743–1753.

43 X. D. Wu, H. N. Yu, D. Weng, S. Liu and J. Fan, *J. Rare Earths*, 2013, **31**, 1141–1147.

44 P. Venkataswamy, D. Jampaiah, F. J. Lin, I. Alxneit and B. M. Reddy, *Appl. Surf. Sci.*, 2015, **349**, 299–309.

45 F. Larachi, J. Pierre, A. Adnot and A. Bernis, *Appl. Surf. Sci.*, 2002, **195**, 236–250.

46 J. Verhelst, D. Decroupet and D. de Vos, *Catal. Sci. Technol.*, 2013, **3**, 1579–1590.

47 J. Wang, J. Z. Zhu, X. X. Zhou, Y. Y. Du, W. M. Huang, J. J. Liu, W. Q. Zhang, J. L. Shi and H. R. Chen, *J. Mater. Chem. A*, 2015, **3**, 7631–7638.

48 D. Jampaiah, K. M. Tur, S. J. Ippolito, Y. M. Sabri, J. Tardio, S. K. Bhargava and B. M. Reddy, *RSC Adv.*, 2013, **3**, 12963–12974.

49 S. Liu, X. D. Wu, D. Weng and R. Ran, *J. Rare Earths*, 2015, **33**, 567–590.

50 P. G. Harrison, I. K. Ball, W. Daniell, P. Lukinskas, M. Cespedes, E. E. Miro and M. A. Ulla, *Chem. Eng. J.*, 2003, **95**, 47–55.

51 Z. P. Wang, M. X. Chen and W. F. Shangguan, *Acta Phys.-Chim. Sin.*, 2009, **25**, 79–85.

52 S. J. Jelles, R. R. Krul, M. Makee and J. A. Moulijn, *Catal. Today*, 1999, **53**, 623–630.